Nanoscale Research Letters

NANO EXPRESS Open Access

Effect of Facile p-Doping on Electrical and Optoelectronic Characteristics of Ambipolar WSe_2 Field-Effect Transistors

Junseok Seo, Kyungjune Cho, Woocheol Lee, Jiwon Shin, Jae-Keun Kim, Jaeyoung Kim, Jinsu Pak* and Takhee Lee*

Abstract

We investigated the electrical and optoelectronic characteristics of ambipolar WSe_2 field-effect transistors (FETs) via facile p-doping process during the thermal annealing in ambient. Through this annealing, the oxygen molecules were successfully doped into the WSe_2 surface, which ensured higher p-type conductivity and the shift of the transfer curve to the positive gate voltage direction. Besides, considerably improved photoswitching response characteristics of ambipolar WSe_2 FETs were achieved by the annealing in ambient. To explore the origin of the changes in electrical and optoelectronic properties, the analyses via X-ray photoelectron, Raman, and photoluminescence spectroscopies were performed. From these analyses, it turned out that WO_3 layers formed by the annealing in ambient introduced p-doping to ambipolar WSe_2 FETs, and disorders originated from the WO_3/WSe_2 interfaces acted as non-radiative recombination sites, leading to significantly improved photoswitching response time characteristics.

Keywords: WSe_2, Ambipolar field-effect transistors, p-doping, Electrical characteristics, Optoelectronic characteristics

Background

Two-dimensional (2D) materials have attracted considerable interest as promising candidates for next-generation electronics and optoelectronic devices [1, 2]. Although graphene is one of the most well-studied 2D materials, it lacks an intrinsic bandgap, restricting its wide application. Meanwhile, 2D transition metal dichalcogenides (TMDs), such as MoS_2, $MoSe_2$, WS_2, and WSe_2, are advantageous in that they can be used as a channel material of field-effect transistors (FETs) due to their intrinsic bandgap properties, good carrier mobility, and high on/off ratio [2, 3]. Hence, TMDs have been widely used in various devices, such as transistors [4–6], sensors [7–10], logic circuits [11], memory devices [12], field-emission devices [13], and photodetectors [14, 15]. In particular, FETs based on WSe_2 have demonstrated great ambipolar characteristics such as high carrier mobilities, outstanding photoresponsive properties, excellent mechanical flexibility, and durability [16–18]. Nevertheless, doping WSe_2 is required to further improve field-effect mobilities or contact properties which are essential in a variety of electronic applications [16, 19]. Among a lot of approaches for doping, thermal annealing in ambient to form WO_3 layers on a WSe_2 surface has been demonstrated to be a facile as well as an efficient p-type doping processes [20–22]. For example, Liu et al. thermally annealed WSe_2 films in ambient without use of additional substances to dope the films in the p-type manner and improved the hole mobility to 83 $cm^2\ V^{-1}\ s^{-1}$ with employing hexagonal boron nitride substrate [20]. However, thorough studies on the optical and optoelectronic characteristics of WSe_2 doped by WO_3 are desired for the optoelectronic applications such as phototransistors, photodiodes, and light-emitting diodes [17, 18, 23, 24].

In this work, we explored the electrical, optical, and optoelectronic properties of ambipolar WSe_2 FETs before and after thermal annealing in ambient. The oxidized layer (WO_3) formed on a WSe_2 surface during the annealing successfully introduced p-doping to the ambipolar WSe_2 FETs, leading to a shift of the transfer curve to the positive gate voltage direction. Interestingly,

* Correspondence: jinsu2060@gmail.com; tlee@snu.ac.kr
Department of Physics and Astronomy, and Institute of Applied Physics, Seoul National University, Seoul 08826, Korea

long-lasting photoconductivity, which is a phenomenon of the conductance's being retained after the light irradiation is turned off, disappeared after the annealing. Furthermore, we performed various experiments, such as X-ray photoelectron spectroscopy (XPS), photoluminescence (PL) spectroscopy, and Raman spectroscopy to investigate the origin of the changes in the electrical and photoswitching characteristics of the ambipolar WSe_2 FETs.

Methods

WSe_2 flakes were prepared by the micromechanical exfoliation method from a bulk WSe_2 crystal, and were transferred to a 270-nm-thick SiO_2 layer on a heavily doped p++ Si wafer (resistivity ~ 5×10^{-3} Ω cm) that was used as the back gate of the FET devices. The thickness of the WSe_2 flakes was measured using an atomic force microscope (NX 10 AFM, Park Systems). To create electrode patterns, we spin-coated poly(methyl methacrylate) (PMMA) 495K (11% concentration in anisole) as an electron resist layer at 4000 rpm. After the spin-coating, the samples were baked on a hot plate at 180 °C for 90 s. We designed the electrode patterns using an electron-beam lithography instrument (JSM-6510, JEOL), and developed the patterns with a methyl isobutyl ketone/isopropyl alcohol (1:3) solution for 120 s. Finally, titanium metal (30-nm-thick) electrodes were deposited using an electron-beam evaporator (KVE-2004L, Korea Vacuum Tech).

Thermal annealing in ambient was performed on a hot plate at certain temperatures. Thermal annealing in vacuum was performed using a rapid thermal annealing system (KVR-4000, Korea Vacuum Tech) at 4.5×10^{-4} Torr and 200 °C for 1 h.

Photoluminescence and Raman spectroscopy measurements were performed using a confocal imaging system (XperRamn 200, Nanobase) with the incident laser wavelength of 532 nm. X-ray photoelectron spectroscopy measurements were performed using an electron energy analyzer (AXIS SUPRA, Kratos). The electrical characteristics of the devices were measured using a probe station (JANIS, ST-500) and a semiconductor parameter analyzer (Keithley 4200-SCS). Photoresponses of the devices were measured under laser (MDE4070V) illumination.

Results and Discussion

Figure 1a shows the optical images of a WSe_2 flake and a fabricated WSe_2 FET. The WSe_2 flake was mechanically exfoliated from a bulk WSe_2 crystal and transferred on a 270-nm-thick SiO_2 surface on a heavily doped p++ Si wafer that was used as the back gate of the FET. Titanium metal patterns used as source and drain electrodes were deposited on the WSe_2 surface. The detailed device fabrication process is explained in the Additional file 1: Figure S1. A schematic of the fabricated ambipolar WSe_2 FET is shown in Fig. 1b. All the electrical and photoswitching properties of WSe_2 FETs were measured

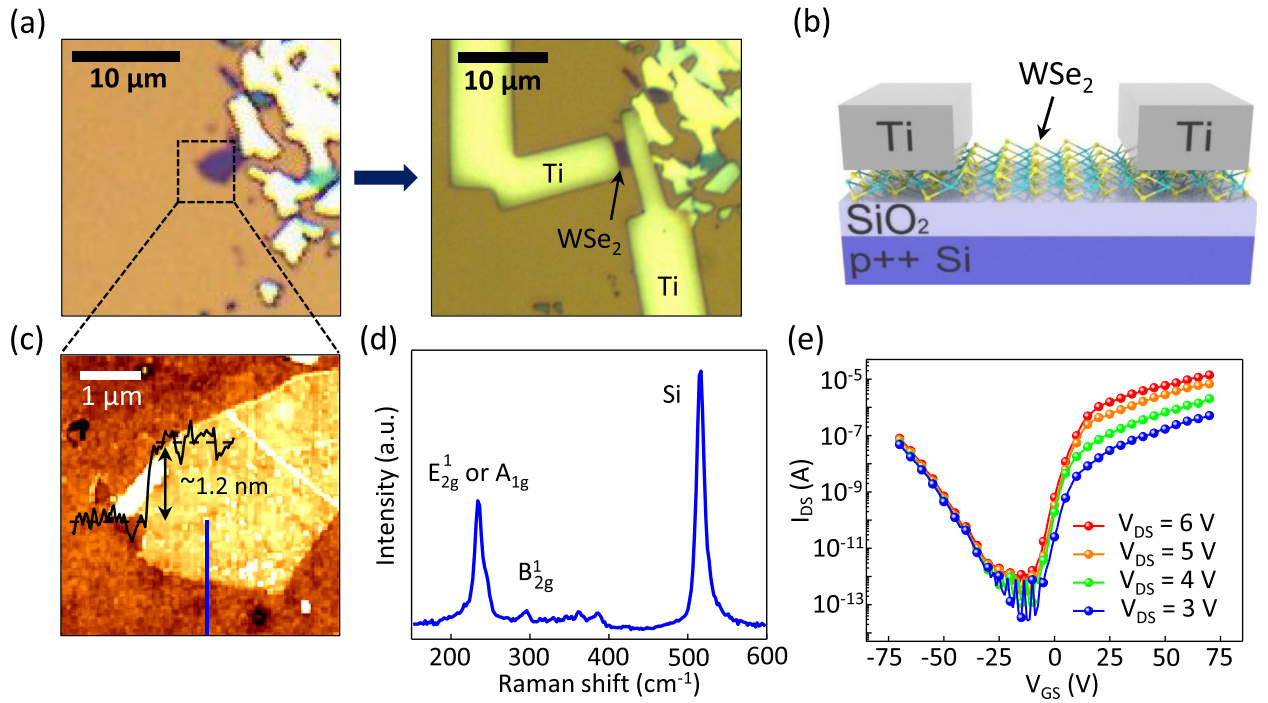

Fig. 1 **a** Optical images of a WSe_2 flake (left) and fabricated WSe_2 FET (right). **b** Schematic of the fabricated WSe_2 FET with Ti contacts. **c** AFM image and **d** Raman spectra of WSe_2. **e** I_{DS}-V_{GS} curves of the ambipolar WSe_2 FET

in vacuum (~ 3.5 × 10^{-3} Torr) since the oxygen and water molecules in the air can affect the properties of the WSe_2 FETs. For instance, it has been reported that the semiconducting type of WSe_2 FETs can be changed from n- to p-type by air exposure [25]. An atomic force microscopy (AFM) image of the WSe_2 flake is displayed in Fig. 1c with the topographic cross-sectional profile. The measured thickness of the WSe_2 flake across the blue line was found to be ~ 1.2 nm (an inset graph in Fig. 1c), corresponding to bilayer WSe_2 (the thickness of a monolayer WSe_2 is ~ 0.7 nm) [16]. Figure 1d displays the Raman spectrum of a WSe_2 showing two clear peaks (the peak at 520 cm^{-1} is assigned to the Si substrate). The Raman peak at 245 cm^{-1} corresponds to the in-plane (E^1_{2g} mode) or out-of-plane (A_{1g} mode) vibrations of WSe_2, and the Raman peak at 308 cm^{-1} corresponds to the B^1_{2g} mode that only appears in multilayer WSe_2 due to the additional interlayer interaction [26]. This finding ensures the good quality of the WSe_2 flake used in these experiments. The E^1_{2g} and A_{1g} peaks of WSe_2 could not be distinguished by the Raman spectroscopy instrument in this study because they are nearly degenerate [27]. Figure 1e shows the transfer curve (source-drain current versus gate voltage; I_{DS}-V_{GS} curve) of the ambipolar WSe_2 FET. Such an ambipolar transport behavior of a WSe_2 FET is due to the number of WSe_2 layers (bilayer) which can determine the major carrier type in FET [28, 29].

Figure 2a shows the I_{DS}-V_{GS} curves of the WSe_2 FET before and after a thermal annealing in ambient at 200 °C for 1 h. The output curves (source-drain current versus source-drain voltage; I_{DS}-V_{DS} curve) of the same WSe_2 FET before and after the annealing are shown in the Additional file 1: Figure S2. Several points are noted here. First, the voltage at which the type of the majority carriers changes ($V_{n\leftrightarrow p}$) shifted from − 15 to − 5 V after the annealing in ambient (represented by the green arrow in Fig. 2a). Second, the I_{DS} increased significantly at the V_{GS} where the majority carriers are holes ($V_{GS} < V_{n\leftrightarrow p}$) and decreased at the V_{GS} where the majority carriers are electrons ($V_{GS} > V_{n\leftrightarrow p}$) after the annealing (represented by the blue arrows in Fig. 2a). This behavior is attributed to the WO_3 layer formed by the annealing that introduces p-doping into the WSe_2 FETs [20]. Third, after the annealing, the hole mobility increased from 0.13 to 1.3 $cm^2\ V^{-1}\ s^{-1}$, and the electron mobility decreased from 5.5 to 0.69 $cm^2\ V^{-1}\ s^{-1}$. We used the formula $\mu = (dI_{DS}/dV_{GS}) \times [L/(WC_iV_{DS})]$ to calculate the carrier mobility, where L (~ 1.5 μm) is the channel length, W (~ 2.8 μm) is the channel width, and $C_i = \varepsilon_0\varepsilon_r/d$ = 1.3 × 10^{-4} F m^{-2} is the capacitance between WSe_2 and the p++ Si wafer per unit area. Here, ε_r (~ 3.9) is the dielectric constant of SiO_2 and d (270 nm) is the thickness of the SiO_2 layer. These changes in the electrical properties after the annealing can be observed more

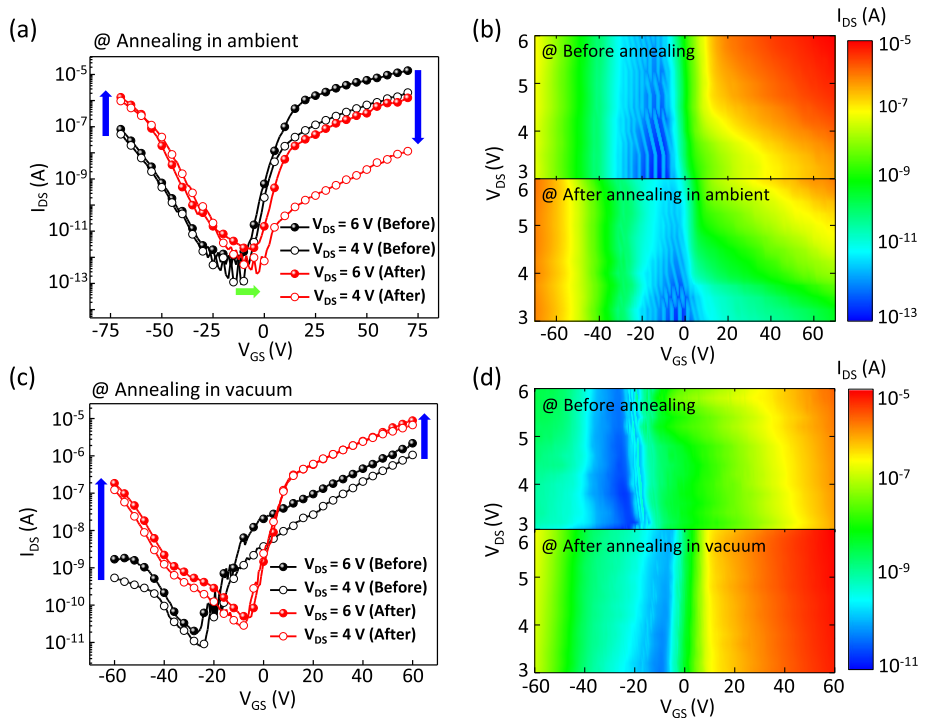

Fig. 2 **a**, **c** I_{DS}-V_{GS} curves on the semilogarithmic scale of a WSe_2 FET before annealing and after annealing at 200 °C for 1 h. **b**, **d** Contour plots of I_{DS} as a function of V_{GS} and V_{DS} before annealing (upper panel) and after annealing at 200 °C for 1 h (lower panel)

clearly in the contour plots that show the I_{DS} as a function of V_{GS} and V_{DS} before (upper panel) and after (lower panel) the annealing in ambient (Fig. 2b). These contour plots were made based on a lot of I_{DS}-V_{GS} curves measured in the V_{GS} range from − 70 to 70 V with a 1.25 V step and V_{DS} range from 3 to 6 V with a 0.25 V step. The blue regions in the contour plots shifted toward the positive V_{GS} direction after the annealing. This shift is consistent with the transfer curve shift shown by the green arrow in Fig. 2a. The change in the color at the positive and negative V_{GS} (Fig. 2b) after the annealing indicates the change in the channel current of the WSe_2 FET (Fig. 2a). Other WSe_2 FETs also showed the same change in the electrical properties after annealing in ambient (see Additional file 1: Figures S3 and S4 in the Additional file). Besides, the change of electrical characteristics by the annealing the WSe_2 FET in vacuum (~ 4.5×10^{-4} Torr) at 200 °C for 1 h was investigated (Fig. 2c, d). In contrast with the results of the FET annealed in ambient, the I_{DS} increased at both V_{GS} conditions of $V_{GS} > V_{n\leftrightarrow p}$ and $V_{GS} < V_{n\leftrightarrow p}$. The increased I_{DS} obtained by annealing in vacuum is attributed to the improved WSe_2-Ti contacts without formation of WO_3 [30]. From the comparison results, it can be anticipated that p-doping was introduced by interaction with the oxygen molecules during the annealing in ambient. The origins of the change in the electrical characteristics are discussed in more detail via the analysis of XPS data afterward.

Next, we measured the photoswitching characteristics of the WSe_2 FET before and after the thermal annealing in ambient (Fig. 3a, b). The electrical characteristics of this FET are shown in the Additional file 1: Figure S3. The laser was irradiated onto the WSe_2 FET and was turned off when the source-drain current appeared to become saturated. Note that the photoswitching experiments were performed at fixed V_{GS} = 0 V, V_{DS} = 10 V, the laser wavelength of 405 nm, and the laser power density of 11 mW/cm^2. Figure 3a, b shows the photoswitching characteristics before and after the annealing in ambient, respectively. In this study, the rise time constant (τ_{rise}) is defined as the time required for the photocurrent (difference between the currents measured in the dark and under irradiation, i.e., $I_{ph} = I_{irra} - I_{dark}$) to change from 10 to 90% of the maximum, and the decay time (τ_{decay}) is the time at which the photocurrent decreases to $1/e$ of its initial value. The purple regions in Fig. 3a, b indicate the time under the laser irradiation. We observed a dramatic change in the photoswitching response times of the WSe_2 FET after the thermal annealing. Both τ_{rise} and τ_{decay} decreased from 92.2 and 57.6 s to less than 0.15 s and 0.33 s, respectively (corresponding to the decrease of more than 610 times and 170 times, respectively). Note that τ_{rise} and τ_{decay} after

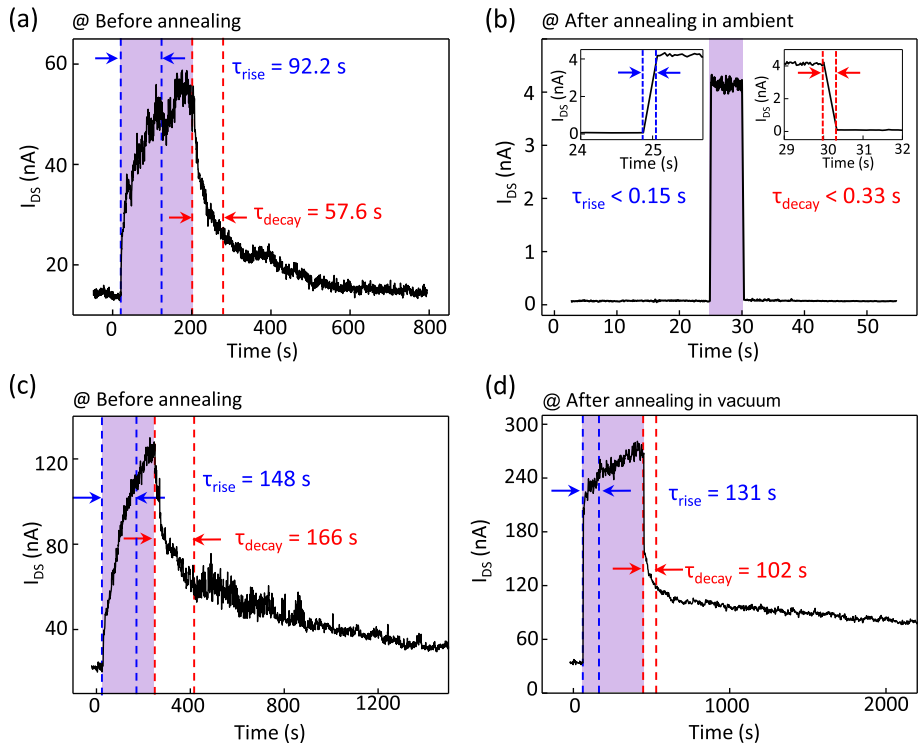

Fig. 3 Photoswitching responses of ambipolar WSe_2 FETs **a**, **c** before and after annealing **b** in ambient at 200 °C for 1 h and **d** in vacuum, respectively. All data were measured at V_{GS} = 0 V and V_{DS} = 10 V

the annealing could not be measured precisely due to instrument limitations. To verify that the change in the photoswitching response times is due to the effect of the oxidation of the WSe_2 layers, we compared the photoswitching behavior of the WSe_2 FET before and after thermal annealing in vacuum (~ 4.5×10^{-4} Torr) at 200 °C for 1 h (Fig. 3c, d). Contrary to the dramatic decrease of the photoswitching response times for the FET annealed in ambient, a relatively small changes of τ_{rise} (from 148 to 131 s) and τ_{decay} (from 166 to 102 s) were observed for the sample annealed in vacuum. This result signifies that the oxidation of the WSe_2 surface by annealing in ambient is a major origin for the fast photoswitching response. The reason of improved photoswitching behavior by annealing in ambient is that the lattice mismatch between the WSe_2 and WO_3 structures provides traps and recombination sites in the bandgap of WSe_2, which can promote the recombination processes of photogenerated carriers.

In addition, for the further investigation on the origin of long-lasting photoswitching characteristics after turning off the laser, the photoswitching characteristics at several V_{GS} were investigated (Fig. 4). The electrical characteristics of this FET are shown in the Additional file 1: Figure S4. The applied V_{GS} = 5 V, V_{GS} = − 15 V, and V_{GS} = − 90 V correspond to the range of $V_{GS} > V_{n\leftrightarrow p}$, $V_{GS} \sim V_{n\leftrightarrow p}$, and $V_{GS} < V_{n\leftrightarrow p}$, respectively. A notable point is that the photoswitching responses strongly relied on the range of V_{GS} whether it was annealed or not. As decreasing V_{GS} from 5 to − 90 V in case of before the annealing, the long-lasting photoconductivity (marked as dotted circles in Fig. 4) disappears at V_{GS} = − 15 V (Fig. 4c) and then reappeared at V_{GS} = − 90 V (Fig. 4e). This V_{GS}-dependent photoswitching characteristics are mainly due to the changed charge carrier dynamics by the applied V_{GS} [31]. Depending on the applied V_{GS} affecting the location of Fermi level (E_F), the amount of injected carriers after turning off the irradiation can be determined (Additional file 1: Figure S5) [31]. We proposed the band diagrams for explaining these complex V_{GS}-dependent photoswitching characteristics in detail when the irradiation is turned on and off (see the section 4 in Additional file 1).

Figure 4a, b shows that photoswitching characteristics became improved at V_{GS} = 5 V ($V_{GS} > V_{n\leftrightarrow p}$) by the thermal annealing, which is in agreement with the results in Fig. 3. This behavior also can be explained by the promoted recombination processes at the induced recombination sites between WSe_2 and WO_3 interface. The PL result demonstrated the existence of non-radiative recombination sites at WO_3/WSe_2, which will be discussed afterward. At V_{GS} = − 15 V ($V_{GS} \sim V_{n\leftrightarrow p}$), we could not observe the distinct change after the thermal annealing due to the highly rapid photoswitching characteristics (Fig. 4c, d). This rapid photoswitching behavior originates from the location of E_F in the middle of WSe_2 bandgap, which suppresses the additional charge

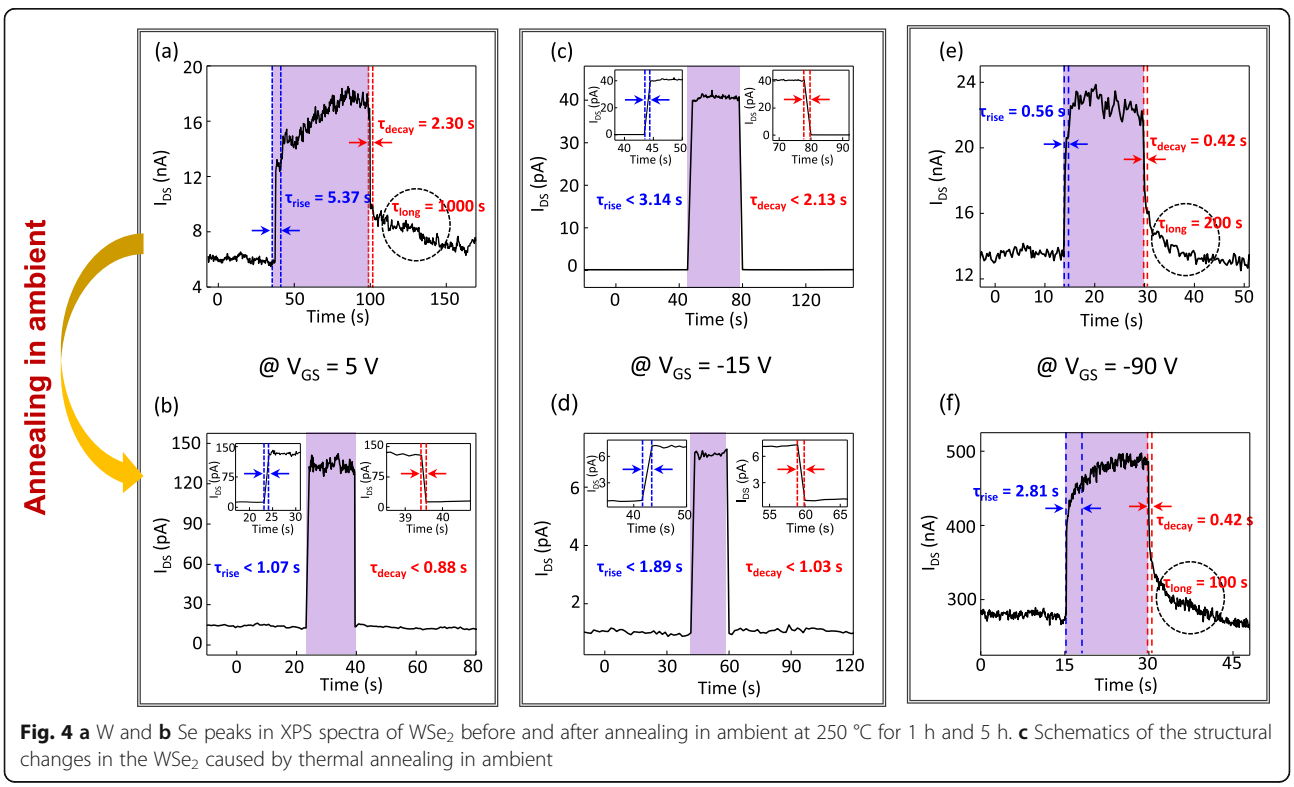

Fig. 4 **a** W and **b** Se peaks in XPS spectra of WSe_2 before and after annealing in ambient at 250 °C for 1 h and 5 h. **c** Schematics of the structural changes in the WSe_2 caused by thermal annealing in ambient

injection after turning off the irradiation (see the section 4 in Additional file 1 for detail). For the case of V_{GS} = − 90 V (Fig. 4e, f), τ_{decay} and τ_{long} were maintained and shortened, respectively, although the current after the annealing was much higher than that before the annealing (more than 20 times). Importantly, there is a trade-off between the photo-induced current and decay time constants in phototransistors, because the trapped photogenerated minority carriers can produce an additional electric field, thereby leading to the increased channel current and demanding continuous charge injection even after the irradiation is turned off [32, 33]. In this regard, the preservation of τ_{decay} and shortened τ_{long} in spite of the significantly increased photo-induced current signifies the improved photoswitching characteristics by the annealing in ambient as shown in Fig. 4e, f. Regarding τ_{rise}, the location of E_F moves to the valence band by p-doping, which causes non-charge neutrality to become stronger due to the decreased hole trap sites where the photogenerated holes can occupy (Additional file 1: Figure S6a). Due to the strong non-charge neutrality, under the irradiation, the more charges are injected for satisfying the charge neutrality. And, photogenerated carriers will undergo more scattering with free carriers while passing through the channel to contribute to the photocurrent, so that τ_{rise} time can become longer. For that reason, the τ_{rise} becomes longer at V_{GS} = − 90 V after thermal annealing as shown in Fig. 4e, f (see the section 4 in Additional file 1 for more detail).

Figure 5a, b shows the XPS analyses to investigate the changes in the elemental composition of the WSe_2 by the thermal annealing in ambient. Although the annealing at 200 °C for 1 h was sufficient to alter both the electrical and photoswitching characteristics as shown in Figs. 2 and 3, these annealing temperature and time were not enough to observe the change in the elemental composition of the WSe_2. Thus, the mechanically exfoliated WSe_2 flakes were annealed at 250 °C for 1 h and 5 h in ambient for XPS analyses as shown in Fig. 5a, b. It should be noted that intensities of the two tungsten peaks (labeled as W^{6+} in Fig. 5a) at the binding energies of 35.5 eV and 37.8 eV gradually increased with increased

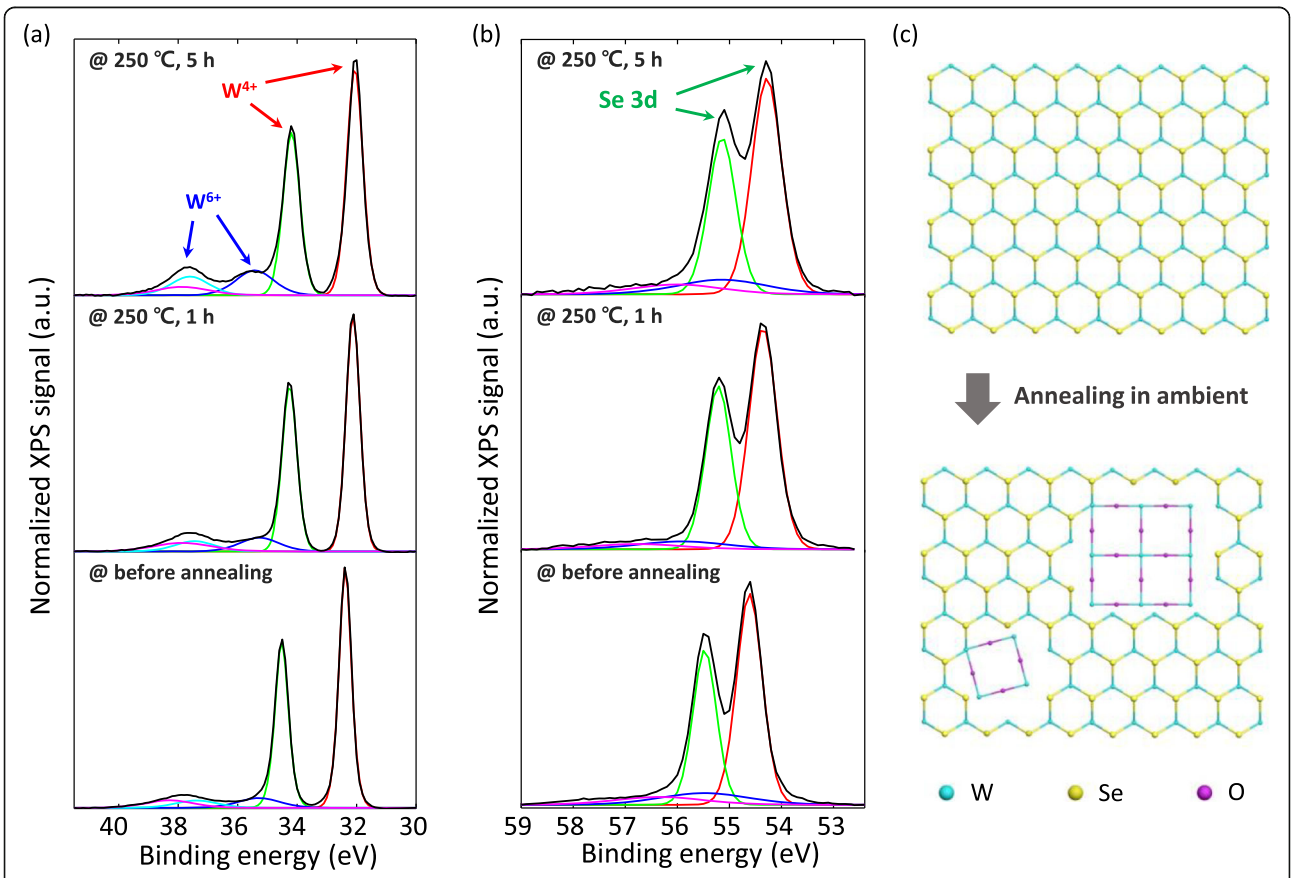

Fig. 5 **a** Raman spectra of the WSe_2 after annealing in ambient at 200 °C for 60 min (black line), at 350 °C for 60 min (red line), and at 500 °C for 5 min (blue line). Inset images correspond to the optical images before and after annealing in 500 °C, respectively. Scale bar = 15 μm. **b** Raman mapping images after annealing at 500 °C integrating with bands at 712 cm^{-1} and 806 cm^{-1}, respectively. Scale bar = 10 μm. **c** Optical bandgap of the WSe_2 before, after annealing in ambient at 250 °C for 30 min, and for 60 min. An inset image is the optical image of a monolayer WSe_2 flake (labeled as sample 1) with scale bar = 10 μm. **d** Maximum PL intensity and corresponding PL mapping images with a scale bar of 10 μm

annealing time, whereas no changes were observed in the intensities of the selenium peaks. The tungsten peaks of W^{6+} generated by the thermal annealing indicate the formation of WO_3 due to the reaction of WSe_2 with oxygen in air during the annealing [20, 34]. On the other hand, the formation of selenium oxides, such as Se_2O_3, was not noticeable (Fig. 5b). Figure 5c exhibits the schematics of microscopic structure before and after WSe_2 oxidation by annealing, and those are drawn based on the actual geometric structure of WSe_2 and cubic WO_3 (W-Se bond length of 2.53 Å, Se-Se bond length of 3.34 Å, and W-O bond length of 1.93 Å) [20, 35, 36]. Since WSe_2 has a hexagonal structure, while WO_3 has a cubic structure, the WSe_2-WO_3 structure is a quilted in-plane heterojunction, as shown in Fig. 5c [20]. Therefore, the origin of the changed electrical properties after the annealing in ambient (Fig. 2a, b) can be explained by the formation of WO_3. The formed WO_3 can serve as an acceptor due to the difference between the work functions of WSe_2 (~ 4.4 eV) and WO_3 (~ 6.7 eV) that gives rise to the increased I_{DS} in the negative V_{GS} region ($V_{GS} < V_{n\leftrightarrow p}$) and the decreased I_{DS} in the positive V_{GS} region ($V_{GS} > V_{n\leftrightarrow p}$) [20, 37, 38]. Similar to our results, there have been several reports that a WO_3 layer which is either deposited on or embedded in a WSe_2 sheet introduced p-doping into a WSe_2 FET [20–22].

We performed Raman and PL spectroscopy experiments to investigate the optical influence by the formation of WO_3. Figure 6a shows Raman spectra of the WSe_2 after the annealing in ambient at 200 °C for 60 min (black line), at 350 °C for 60 min (red line), and at 500 °C for 5 min (blue line). The appearance of new peaks around 712 cm^{-1} and 806 cm^{-1} by the annealing at 500 °C, which are very close to the Raman peaks of WO_3 (709 cm^{-1} and 810 cm^{-1}) [39], support the formation of WO_3 layer on WSe_2 surface. Inset images are the

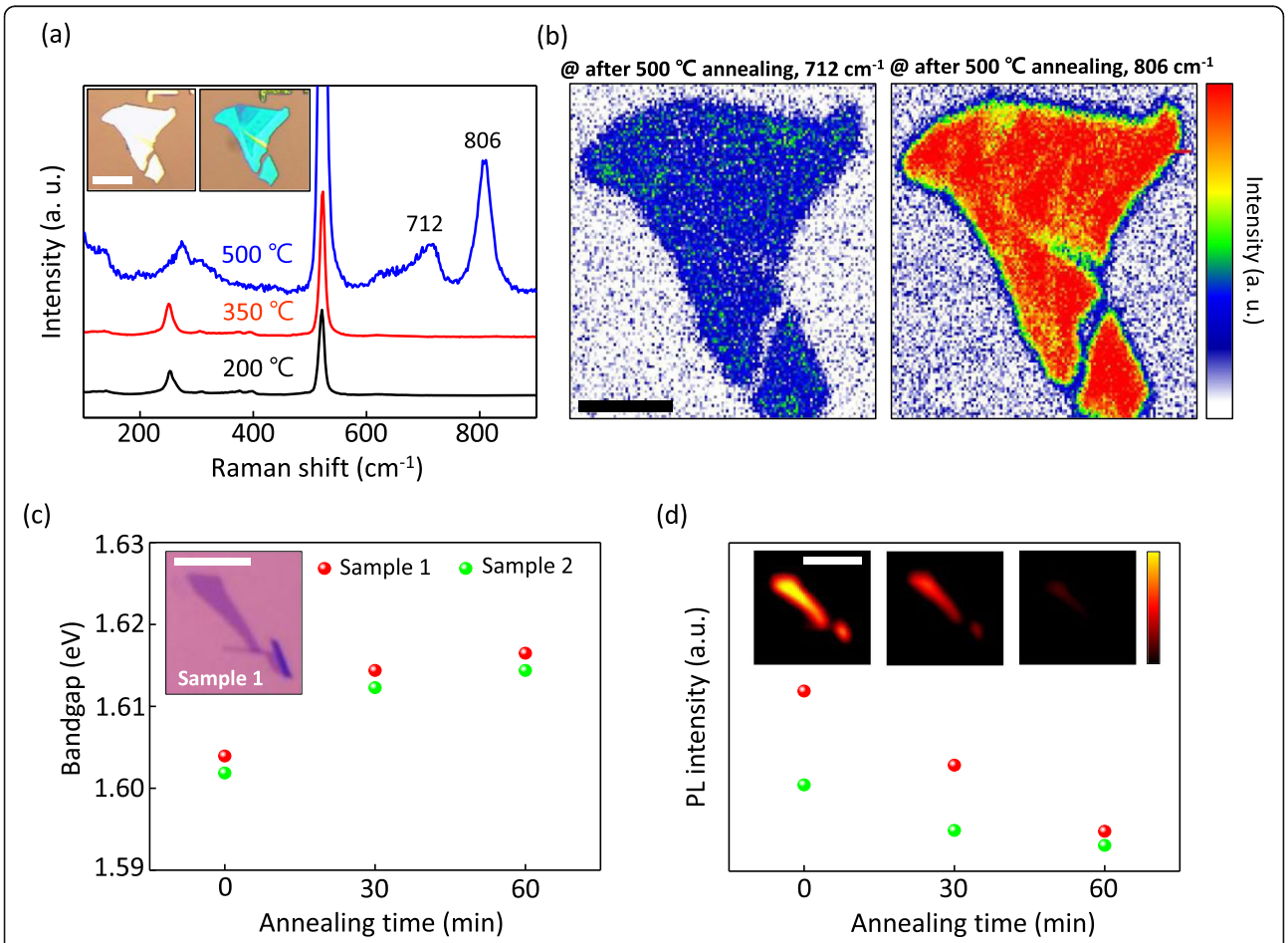

Fig. 6 **a** Raman spectra of the WSe_2 after annealing in ambient at 200 °C for 60 min (black line), at 350 °C for 60 min (red line), and at 500 °C for 5 min (blue line). Inset images correspond to the optical images before and after annealing in 500 °C, respectively. Scale bar = 15 μm. **b** Raman mapping images after annealing at 500 °C integrating with bands at 712 cm^{-1} and 806 cm^{-1}, respectively. Scale bar = 10 μm. **c** Optical bandgap of the WSe_2 before, after annealing in ambient at 250 °C for 30 min, and for 60 min. An inset image is the optical image of a monolayer WSe_2 flake (labeled as sample 1) with scale bar = 10 μm. **d** Maximum PL intensity and corresponding PL mapping images with a scale bar of 10 μm

optical images before and after the annealing at 500 °C for 5 min. Raman mapping images integrating with the bands of 712 cm^{-1} and 806 cm^{-1} in Fig. 6b show the uniform WO_3 formation on WSe_2 surface.

PL spectroscopy analysis was conducted for two different monolayer WSe_2 flakes (labeled as sample 1 and sample 2) as shown in Fig. 6c. The inset of Fig. 6c corresponds to an optical image of sample 1. Each WSe_2 flakes were annealed for 30 min and 60 min at 250 °C in ambient. The optical and PL mapping images of the other monolayer WSe_2 flake (labeled as sample 2) are provided in the Additional file 1: Figure S7. As the annealing time increased, the optical bandgaps of the WSe_2 became wider. The optical bandgap was extracted from the photon energy of the maximum intensity in PL spectrum because that corresponds to the resonance fluorescence originating from the bandgap. While the optical bandgap of the sample 1 was measured as ~ 1.60 eV before the annealing corresponding to the bandgap of monolayer WSe_2 [27], the bandgap value changed to ~ 1.61 eV after the annealing for 60 min. Although the increase (~ 10 meV) of the optical bandgap is slight, this phenomenon can be explained by the formation of the WSe_2-WO_3 in-plane heterojunctions and the dielectric screening effect. Since WO_3 has a larger bandgap of 2.75 eV compared to WSe_2 (1.60 eV for a monolayer) [40], the optical bandgap of the monolayer WSe_2 flakes increased through the annealing in ambient. Furthermore, the formation of WO_3 on WSe_2 can generate a stronger dielectric screening effect due to the larger dielectric constant of WO_3 (~ 90) compared to that of WSe_2 (~ 22) [41, 42]. Consequently, the stronger dielectric screening effect leads to the diminished exciton binding energy and slightly increased the optical bandgap during the thermal annealing [43].

Interestingly, in perspective of the PL intensity, it obviously decreased as the annealing time increased as shown in Fig. 6d. The PL quenching behavior of monolayer WSe_2 can be easily observed in PL mapping images integrating the PL intensity in peak region, as increasing annealing time (inset of Fig. 6d). A similar phenomenon was observed in the MoS_2 treated by oxygen plasma [44]. These results can be explained as follows. Since WO_3 has an indirect bandgap [40], the band structure of WSe_2 may be partially changed to that with an indirect bandgap, which leads to reduced PL intensity. Additionally, the lattice mismatch between the WSe_2 and WO_3 structures provides traps and recombination sites in the bandgap of WSe_2 that can affect the electrical and optical characteristics of the WSe_2. For instance, disorder, defects, and sulfur vacancies can produce shallow or deep trap sites in the MoS_2 layers, giving rise to the recombination process [31, 45]. Therefore, as the annealing time increased, disorder and the defects originating from the lattice mismatch of the WSe_2-WO_3 structure lead to non-radiative (Shockley-Read-Hall) recombination [45], and to reduced PL intensity. Collectively, the experimental results of the XPS, Raman, and PL spectroscopies demonstrate the formation of WO_3 on the WSe_2 surface by the annealing in ambient, and those are in agreement well with recent researches on the oxidation of 2D materials [20, 46]. Besides, from the analysis of PL spectroscopy, it was supported that non-radiative recombination sites induced by WO_3 layer could contribute to the improved photoswitching characteristics by promoting the recombination processes.

Conclusions

In summary, we fabricated ambipolar WSe_2 FETs and studied the electrical properties and photoswitching responses before and after thermal annealing in ambient. We observed that the WSe_2 FETs were successfully doped in the p-type manner and that the photoswitching responses became considerably faster after the ambient thermal annealing. The XPS, Raman, and PL studies demonstrated that the WO_3 layer formed on the WSe_2 surface can play the roles of a p-doping layer and non-radiative recombination sites to promote faster photoswitching behavior. This study provides a deeper understanding of effects on electrical and optoelectronic characteristics of ambipolar WSe_2 FETs by the facile p-doping process via the thermal annealing in ambient.

Additional file

Additional file 1: Figure S1. Schematics of fabricating processes of WSe_2 FET. **Figure S2.** I_{DS}-V_{DS} curves of the WSe_2 FET a when positive V_{GS} applied and b when negative V_{GS} applied. Filled and open circular symbols correspond to the curves before and after annealing in ambient, respectively. **Figure S3.** a Transfer curves (I_{DS}-V_{GS}) before (black symbols) and after (red symbols) annealing in ambient. An inset image shows the optical images of the fabricated WSe_2 FET. b Contour plots which show I_{DS} as a function of V_{GS} and V_{DS} before (upper panel) and after (lower panel) annealing in ambient at 200 °C for 1 h. **Figure S4.** a An optical image of a WSe_2 FET. b An AFM image (left) of the WSe_2 flake and the topographic cross-sectional profile along the blue line (right). Scale bar: 1 μm. c I_{DS}-V_{GS} curves of ambipolar WSe_2 FET before annealing and after annealing in ambient at 200 °C for 1 h. **Figure S5.** Energy band diagrams describing photoswitching dynamics when the irradiation is turned on at a $V_{GS} > V_{n\leftrightarrow p}$, b $V_{GS} \sim V_{n\leftrightarrow p}$, c $V_{GS} < V_{n\leftrightarrow p}$, and after the irradiation is turned off d-f. **Figure S6.** Energy band diagrams before and after p-doping by WO_3 under the irradiation at a $V_{GS} < V_{n\leftrightarrow p}$ and b $V_{GS} > V_{n\leftrightarrow p}$. **Figure S7.** a An optical image of a monolayer WSe_2 flake (Sample 2). b PL mapping images before annealing (left), after annealing in ambient at 250 °C for 30 min (middle) and 60 min (right). (DOCX 2529 kb)

Abbreviations

2D: Two-dimensional;; AFM: Atomic force microscopy; FET: Field-effect transistor;; PL: Photoluminescence;; TMDs: Transition metal dichalcogenides;; XPS: X-ray photoelectron spectroscopy;

Acknowledgments

Not applicable.

Authors' Contributions

TL and JP supervised the experiments and characterization. JS (Junseok Seo) designed and carried out the experiments. KC and WL helped to analyze the results of the electrical and optoelectronic characterization. JS (Jiwon Shin), J-KK, and JK helped to fabricate WSe_2 FETs. JS (Junseok Seo), JP, and TL contributed to writing and editing the manuscript, and all authors contributed to the data analysis and discussion of the results. All authors read and approved the final manuscript.

Funding

The authors appreciate the financial support of the National Creative Research Laboratory program (Grant No. 2012026372) through the National Research Foundation of Korea funded by the Korean Ministry of Science and ICT.

Availability of Data and Materials

All data are fully available without restriction.

Competing Interests

The authors declare that they have no competing interests.

Received: 4 July 2019 Accepted: 21 August 2019
Published online: 12 September 2019

References

1. Novoselov KS, Jiang D, Schedin F, Booth TJ, Khotkevich VV, Morozov SV, Geim AK (2005) Two-dimensional atomic crystals. Proc Natl Acad Sci USA 102:10451–10453
2. Jariwala D, Sangwan VK, Lauhon LJ, Marks TJ, Hersam MC (2014) Emerging device applications for semiconducting two-dimensional transition metal dichalcogenides. ACS Nano 8:1102–1120
3. Mak KF, Lee C, Hone J, Shan J, Heinz TF (2010) Atomically thin MoS_2: a new direct-gap semiconductor. Phys Rev Lett 105:136805
4. Cho K, Park W, Park J, Jeong H, Jang J, Kim TY, Hong WK, Hong S, Lee T (2013) Electric stress-induced threshold voltage instability of multilayer MoS_2 field effect transistors. ACS Nano 7:7751–7758
5. Kim S, Konar A, Hwang WS, Lee JH, Lee J, Yang J, Jung C, Kim H, Yoo JB, Choi JY, Jin YW, Lee SY, Jena D, Choi W, Kim K (2012) High-mobility and low-power thin-film transistors based on multilayer MoS_2 crystals. Nat Commun 3:1011
6. Lee GH, Cui X, Kim YD, Arefe G, Zhang X, Lee CH, Ye F, Watanabe K, Taniguchi T, Kim P, Hone J (2015) Highly stable, dual-gated MoS_2 transistors encapsulated by hexagonal boron nitride with gate-controllable contact, resistance, and threshold voltage. ACS Nano 9:7019–7026
7. Liu B, Chen L, Liu G, Abbas AN, Fathi M, Zhou C (2014) High-performance chemical sensing using Schottky-contacted chemical vapor deposition grown monolayer MoS_2 transistors. ACS Nano 8:5304–5314
8. Zhou Y, Zou C, Lin X (2018) UV light activated NO_2 gas sensing based on Au nanoparticles decorated few-layer MoS_2 thin film at room temperature. Appl. Phys. Lett. 113:082103
9. Zhou Y, Gao C, Guo Y (2018) UV assisted ultrasensitive trace NO_2 gas sensing based on few-layer MoS_2 nanosheet-ZnO nanowire heterojunctions at room temperature. J. Mater. Chem. A 6:10286–10296
10. Zhou Y, Li X, Wang Y, Hai H, Guo Y (2019) UV illumination-enhanced molecular ammonia detection based on a ternary-reduced graphene oxide-titanium dioxide-Au composited film at room temperature. 91:3311-3318
11. Radisavljevic B, Whitwick MB, Kis A (2011) Integrated circuits and logic operations based on single-layer MoS_2. ACS Nano 5:9934–9938
12. Roy K, Padmanabhan M, Goswami S, Si TP, Ramalingam G, Raghavan S, Ghosh A (2013) Graphene-MoS_2 hybrid structures for multifunctional photoresponsive memory devices. Nat Nanotechnol 8:826–830
13. Bartolomeo AD, Urban F, Passacantando M, McEvoy N, Peters L, Iemmo L, Luongo G, Romeo F, Giubileo F (2019) A WSe_2 vertical field emission transistor. Nanoscale 11:1538–1548
14. Lopez-Sanchez O, Lembke D, Kayci M, Radenovic A, Kis A (2013) Ultrasensitive photodetectors based on monolayer MoS_2. Nat Nanotechnol 8:497–501
15. Pak J, Jang J, Cho K, Kim TY, Kim JK, Song Y, Hong WK, Min M, Lee H, Lee T (2015) Enhancement of photodetection characteristics of MoS_2 field effect transistors using surface treatment with copper phthalocyanine. Nanoscale 7:18780–18788
16. Fang H, Chuang S, Chang TC, Takei K, Takahashi T, Javey A (2012) High-performance single layered WSe_2 p-FETs with chemically doped contacts. Nano Lett 12:3788–3792
17. Zhang W, Chiu MH, Chen CH, Chen W, Li LJ, Wee ATS (2014) Role of metal contacts in high-performance phototransistors based on WSe_2 monolayers. ACS Nano 8:8653–8661
18. Zheng Z, Zhang T, Yao J, Zhang Y, Xu J, Yang G (2016) Flexible, transparent and ultra-broadband photodetector based on large-area WSe_2 film for wearable devices. Nanotechnology 27:225501
19. Chen CH, Wu CL, Pu J, Chiu MH, Kumar P, Takenobu T, Li LJ (2014) Hole mobility enhancement and p-doping in monolayer WSe_2 by gold decoration. 2D Mater 1:034001
20. Liu B, Ma Y, Zhang A, Chen L, Abbas AN, Liu Y, Shen C, Wan H, Zhou C (2016) High-performance WSe_2 field-effect transistors via controlled formation of in-plane heterojunctions. ACS Nano 10:5153–5160
21. Yamamoto M, Dutta S, Aikawa S, Nakaharai S, Wakabayashi K, Fuhrer MS, Ueno K, Tsukagoshi K (2015) Self-limiting layer-by-layer oxidation of atomically thin WSe_2. Nano Lett 15:2067–2073
22. Yamamoto M, Nakaharai S, Ueno K, Tsukagoshi K (2016) Self-limiting oxides on WSe_2 as controlled surface acceptors and low-resistance hole contacts. Nano Lett 16:2720–2727
23. Lin P, Zhu L, Li D, Xu L, Pan C, Wang Z (2018) Piezo-phototronic effect for enhanced flexible MoS_2/WSe_2 van der Waals photodiodes. Adv Funct Mater 28:1802849
24. Cheng R, Li D, Zhou H, Wang C, Yin A, Jiang S, Liu Y, Chen Y, Huang Y, Duan X (2014) Electroluminescence and photocurrent generation from atomically sharp WSe_2/MoS_2 heterojunction p-n diodes. Nano Lett 14:5590–5597
25. Urban F, Martucciello N, Peters L, McEvoy N, Bartolomeo AD (2018) Environmental effects on the electrical characteristics of back-gated WSe_2 field-effect transistors. Nanomaterials 8:901
26. Li H, Lu G, Wang Y, Yin Z, Cong C, He Q, Wang L, Ding F, Yu T, Zhang H (2013) Mechanical exfoliation and characterization of single- and few-layer nanosheets of WSe_2, TaS_2, and $TaSe_2$. Small 9:1974–1981
27. Sahin H, Tongay S, Horzum S, Fan W, Zhou J, Li J, Wu J, Peeters FM (2013) Anomalous Raman spectra and thickness-dependent electronic properties of WSe_2. Phys Rev B 87:165409
28. Pudasaini PR, Oyedele A, Zhang C, Stanford MG, Cross N, Wong AT, Hoffman AN, Xiao K, Duscher G, Mandrus DG, Ward TZ, Rack PD (2018) High-performance multilayer WSe_2 field-effect transistors with carrier type control. Nano Res 11:722–730
29. Zhou C, Zhao Y, Raju S, Wang Y, Lin Z, Chan M, Chai Y (2016) Carrier type control of WSe_2 field-effect transistors by thickness modulation and MoO_3 layer doping. Adv Funct Mater 26:4223–4230
30. Qiu H, Pan L, Yao Z, Li J, Shi Y, Wang X (2012) Electrical characterization of back-gated bi-layer MoS_2 field-effect transistors and the effect of ambient on their performances. Appl Phys Lett 100:123104
31. Kufer D, Konstantatos G (2015) Highly sensitive, encapsulated MoS_2 photodetector with gate controllable gain and speed. Nano Lett 15:7307–7313
32. Fang H, Hu W (2017) Photogating in low dimensional photodetectors. Adv Sci 4:1700323
33. Buscema M, Island JO, Groenendijk DJ, Blanter SI, Steele GA, van der Zant HSJ, Castellanos-Gomez A (2015) Photocurrent generation with two-dimensional van der Waals semiconductors. Chem. Sov. Rev. 44:3691–3718
34. Alov NV (2015) XPS study of MoO_3 and WO_3 oxide surface modification by low-energy Ar^+ ion bombardment. Status Solidi C 12:263–266
35. Schutte WJ, Doer JKD, Jellinek F (1987) Crystal structures of tungsten disulfide and diselenide. J Solid State Chem 70:207–209
36. Bullett DW (1983) Bulk and surface electron states in WO_3 and tungsten bronzes. J Phys C: Solid State Phys 16:2197–2207
37. Smyth CM, Addou R, McDonnell S, Hinkle CL, Wallace RM (2017) WSe_2-contact metal interface chemistry and band alignment under high vacuum and ultra high vacuum deposition conditions. 2D Mater 4:025084
38. Meyer J, Hamwi S, Kroger M, Kowalsky W, Riedl T, Kahn A (2012) Transition metal oxides for organic electronics: energetics, device physics and applications. Adv Mater 24:5408–5427
39. Kalantar-zadeh K, Vijayaraghavan A, Ham MH, Zheng H, Breedon M, Strano MS (2010) Synthesis of atomically thin WO_3 sheets from hydrated tungsten trioxide. Chem Mater 22:5560–5566
40. Gonzalez-Borrero PP, Sato F, Medina AN, Baesso ML, Bento AC, Baldissera G, Persson C, Nikalsson GA, Granqvist CG, da Silva AF (2010) Optical ban-gap determination of nanostructured WO_3 film. Appl Phys Lett 96:061909

41. Mansingh A, Sayer M, Webb JB (1978) Electrical conduction in amorphous WO_3 films. J Non-Cryst Solids 28:123–137
42. Li Y, Chernikov A, Zhang X, Rigosi A, Hill HM, van der Zande AM, Chenet DA, Shih EM, Hone J, Heinz TF (2014) Measurement of the optical dielectric function of monolayer transition-metal dichalcogenides: MoS_2, $MoSe_2$, WS_2, and WSe_2. Phys Rev B 90:205422
43. Lin Y, Ling X, Yu L, Huang S, Hsu AL, Lee YH, Kong J, Dresselhaus MS, Palacios T (2014) Dielectric screening of excitons and trions in single-layer MoS_2. Nano Lett 14:5569–5576
44. Kang N, Paudel HP, Leuenberger MN, Tetard L, Khondaker SI (2014) Photoluminescence quenching in single-layer MoS_2 via oxygen plasma treatment. J Phys Chem C 118:21258–21262
45. Furchi MM, Polyushkin DK, Pospischil A, Mueller T (2014) Mechanisms of photoconductivity in atomically thin MoS_2. Nano Lett 14:6165–6170
46. Liu Y, Tan C, Chou H, Nayak A, Wu D, Ghosh R, Chang HY, Hao Y, Wang X, Kim JS, Piner R, Ruoff RS, Akinwande D, Lai K (2015) Thermal oxidation of WSe_2 nanosheets adhered on SiO_2/Si substrates. Nano Lett 15:4979–4984

Publisher's Note